

Effect of stones on the sand saltation threshold during natural sand and dust storms in a stony desert in Tsogt-Ovoo in the Gobi Desert, Mongolia

Batjargal BUYANTOGTOKH^{1,2*}, Yasunori KUROSAKI¹, Atsushi TSUNEKAWA¹, Mitsuru TSUBO¹, Batdelger GANTSETSEG², Amarsaikhan DAVAADORJ², Masahide ISHIZUKA³, Tsuyoshi T SEKIYAMA⁴, Taichu Y TANAKA⁴, Takashi MAKI⁴

¹ Arid Land Research Center, Tottori University, Tottori 680-0001, Japan;

² Information and Research Institute of Meteorology, Hydrology and Environment, Ulaanbaatar 15160, Mongolia;

³ Faculty of Engineering and Design, Kagawa University, Takamatsu 761-0396, Japan;

⁴ Meteorological Research Institute, Japan Meteorological Agency, Tsukuba 305-0052, Japan

Abstract: Non-erodible elements such as stones and vegetation are key to controlling wind erosion and dust emission in drylands. Stony deserts are widely distributed in the Gobi Desert, but the effect of stones on wind erosion and dust emission have not been well studied, except under artificial conditions. In this study, we evaluated the effect of stones on wind erosion and dust emission by measuring the sand saltation threshold in a stony desert in Tsogt-Ovoo in the Gobi Desert, Mongolia, under natural surface conditions during sand and dust storms. We quantified the amount of stones by measuring the roughness density, and determined the threshold friction velocity for sand saltation by measuring wind speed and sand saltation count. Our results showed that the threshold friction velocity increased with the roughness density of stones. In the northern part of the study area, where neither a surface crust nor vegetation was observed, the roughness density of stones was 0.000 in a topographic depression (TD), 0.050 on a northern slope (N.SL), and 0.160 on the northern mountain (N.MT). The mean threshold friction velocity values were 0.23, 0.41, and 0.57 m/s at the TD, N.SL, and N.MT sites, respectively. In the southern part of the study area, the roughness density values of stones were 0.000 and 0.070–0.320 at the TD and southern slope sites, respectively, and the mean threshold friction velocities were 0.23 and 0.45–0.71 m/s, respectively. We further compared the observed threshold friction velocities with simulated threshold friction velocities using Raupach's theoretical roughness correction and the measured roughness density values, and found that Raupach's roughness correction worked very well in the simulation of threshold friction velocity in the stony desert. This means that the results of our stone measurement can be applied to a numerical dust model.

Keywords: arid region; threshold friction velocity; roughness density; shear stress; sand saltation threshold; roughness correction; Gobi Desert

Citation: Batjargal BUYANTOGTOKH, Yasunori KUROSAKI, Atsushi TSUNEKAWA, Mitsuru TSUBO, Batdelger GANTSETSEG, Amarsaikhan DAVAADORJ, Masahide ISHIZUKA, Tsuyoshi T SEKIYAMA, Taichu Y TANAKA, Takashi MAKI. 2021. Effect of stones on the sand saltation threshold during natural sand and dust storms in a stony desert in Tsogt-Ovoo in the Gobi Desert, Mongolia. *Journal of Arid Land*, 13(7): 653–673. <https://doi.org/10.1007/s40333-021-0072-7>

*Corresponding author: Batjargal BUYANTOGTOKH (E-mail: buya_9@yahoo.com)

Received 2020-12-21; revised 2021-05-23; accepted 2021-05-29

© Xinjiang Institute of Ecology and Geography, Chinese Academy of Sciences, Science Press and Springer-Verlag GmbH Germany, part of Springer Nature 2021

1 Introduction

Sand and dust storms can cause human and animal mortality (Mu et al., 2013) and health deterioration (Onishi et al., 2015), as well as agricultural production losses (Yang et al., 2002). Additionally, aeolian dust particles that originate from such storms have an impact on climate, though the scale of that impact is still under debate (e.g., Boucher et al., 2013). To avoid damage from storms and to evaluate their effects, a high-precision three-dimensional numerical dust cycle model is needed because of the large uncertainty in the amount of dust emission of current models, which shows an 11.1-fold difference in global dust emission (Wu et al., 2020). Many factors influence erodibility and dust emission. Factors affecting the susceptibility of soil and land surfaces to wind erosion include the presence and coverage of stones, soil particle size, the presence of a soil crust, soil wetness, and the amounts of snow cover and vegetation (Kurosaki et al., 2011a). The effects of these factors on the occurrence of sand and dust storms in East Asia, one of the world's major dust sources, have been evaluated by using an erodibility index, such as the threshold wind friction velocity, and dust occurrence ratios (Kurosaki et al., 2011a, b; Wu et al., 2016, 2020). However, the effect of stones has not been evaluated under natural conditions in East Asia. The Gobi Desert in northern China and southern Mongolia, along with the Taklimakan Desert in Northwest China, is a major dust source in East Asia (e.g., Natsagdorj et al., 2003; Wang et al., 2008; Chen et al., 2017). The Gobi Desert is characterized by widely distributed stone pavements (Cooke, 1970). An area covered by a stone pavement is referred to as a "gobi", which means "stony desert" in Chinese, but in Mongolian, "gobi" is used for a "desert with sparse vegetation, barren soil, and scarce surface water".

Aeolian sand saltation is a key dust emission process (Greeley and Iversen, 1985; Shao et al., 1993). The threshold value of wind friction velocity for sand saltation depends on many parameters, including soil particle size (Gillette et al., 1980; Shao and Lu, 2000; Edwards and Namikas, 2015), the presence of non-erodible elements (Gillette, 1978; Marticorena et al., 2006; Tan et al., 2019), soil moisture (Ishizuka et al., 2009), soil crust (Gillette et al., 1982; Marticorena et al., 1997a), and other soil properties (Gillette, 1988). Non-erodible roughness elements, which include vegetation, stones, and soil crusts, influence the major physical processes involved in wind erosion (Callot et al., 2000) through two effects: the coverage effect and the shear stress (i.e., drag) partitioning effect (Marshall, 1971; Iversen et al., 1990). In quantitative terms, increased coverage of non-erodible elements, by reducing the total erodible area, reduces the sand saltation amount. Similarly, the partitioning of the total shear stress due to wind into the force exerted on the roughness elements and that exerted on intervening surfaces (Schlichting, 1936) reduces the wind shear stress that reaches the soil surface (Gillies et al., 2007) and increases the sand saltation threshold. Li et al. (2020) have shown that variation of sand saltation threshold is due to the different shear stresses caused by the presence of non-erodible elements.

Several theoretical models have been developed to describe the partitioning of shear stress between the surface and roughness elements (Raupach, 1992; Raupach et al., 1993; Marticorena and Bergametti, 1995). Specifically, these models describe the effect of roughness elements on the threshold friction velocity, which is the minimum friction velocity required to initiate movement of sand particles. In dust models, the frequency of sand and dust events is determined by how often the wind velocity exceeds the threshold friction velocity, and their intensity depends on by how much the threshold is exceeded (Callot et al., 2000). The model developed by Raupach et al. (1993) accounts for the effects of roughness elements and their coverage on the threshold friction velocity (Webb et al., 2020) by using the roughness density, which is defined here as the sum of the element frontal areas (i.e., facing the wind direction) divided by the ground surface area, and constant parameters such as the basal-to-frontal area ratio of non-erodible elements. In general, the model by Raupach et al. (1993) performs well with respect to the results of wind tunnel experiments (Gillies et al., 2000), field experiments conducted with artificial cylindrical roughness elements (Gillies et al., 2007), and field experiments conducted in vegetated areas (e.g., King et al., 2005; Gillette et al., 2006).

To investigate the effects of two types of roughness elements, i.e., solid elements (e.g.,

gravel, stone) and flexible elements (e.g., vegetation), on the threshold friction velocity, Marticorena et al. (1997b) developed a double shear stress partition model based on the single shear stress partition model of Marticorena et al. (1997a), and Darmonova et al. (2009) developed a double shear stress partition model based on the model of Raupach et al. (1993). Darmonova et al. (2009) used their model to simulate dust transport over East Asia, as did Xi and Sokolik (2015), Foroutan et al. (2017), and Lee and Park (2020) using the same model. All of the above-mentioned model studies employed representative roughness density of stones for each land cover type because data on the roughness density of a natural stone surface covering wide areas of the world were not available. For example, the minimum roughness density of solid elements is constant in barren and sparsely vegetated land, which is the dominant land cover type in our study area (Tsogt-Ovoo in the Gobi Desert, Mongolia). We question whether accurate results can be obtained by using a constant representative roughness density for natural stones to estimate the threshold friction velocity in this study.

The effects of stones on wind erosion in the Gobi Desert of northern China have been studied mainly by field wind tunnel measurements (e.g., Tan et al., 2013; Zhang et al., 2014; Zhang et al., 2015; Zhang et al., 2016). In these above-mentioned studies, stone coverage was strongly correlated with the threshold friction velocity, and the sand flux decreased exponentially with stone coverage. However, these studies did not consider the effect of the roughness density of stones on the threshold velocity. Recently, Tan et al. (2019) conducted a wind tunnel experiment in the Gobi Desert for aeolian saltation to determine the threshold wind velocities for artificial stony surfaces with different roughness densities and revealed that the threshold friction velocity for sand saltation increased with the roughness density of stones. Their results agree well with the model of Raupach et al. (1993).

Field-based, wind tunnel, and model simulation studies have all shown that the aerodynamic roughness length and roughness density of non-erodible elements are important parameters for assessing the effect of surface roughness elements on the threshold friction velocity in wind erosion models. However, roughness elements are generally described only by their roughness density (Marticorena et al., 1997b). There is a good relation between the ratio of aerodynamic roughness length to the mean height of roughness elements and roughness density (Marshall, 1971; Lancaster and Baas, 1998; King et al., 2005; Marticorena et al., 2006; Hébrard et al., 2012). Thus, for natural stones, if the roughness density and the mean height are well quantified, then the aerodynamic roughness length can be obtained by using the aforementioned relation and could be used in wind erosion models. Therefore, in this study, we measured the roughness density of stones and the observed sand saltation thresholds in Tsogt-Ovoo in the Gobi Desert, Mongolia. We also used the model of Raupach et al. (1993), which includes a roughness correction, to simulate threshold friction velocity using the measured roughness density of stones. The main objective of this research was to evaluate the effects of stones on the threshold friction velocity for sand saltation. The specific objectives were as follows: (1) to quantify roughness density for different coverages, numbers, and sizes of stones; (2) to calculate the threshold friction velocity using observed sand saltation count data and meteorological data; and (3) to validate the theoretical model with roughness correction by simulating threshold friction velocity using the measured roughness density of stones.

2 Study area and methodology

2.1 Study area

Sand and dust storms are a common phenomenon in Asian drylands such as the Gobi Desert and Taklimakan Desert. Our study sites are located in Tsogt-Ovoo Village (44°23'04"N, 105°16'59"E), South Gobi Province, Mongolia, which is in the northern part of the Gobi Desert (Ishizuka et al., 2012). An analysis of meteorological observatory data has shown that Tsogt-Ovoo experiences the highest frequency of dust storms in East Asia (Kurosaki and Mikami, 2007). The area around Tsogt-Ovoo includes a topographic depression that extends

approximately 10 km in the northeast-southwest direction and 20 km in the northwest-southeast direction (Fig. 1). Further, the vegetation coverage in Tsogt-Ovoo differs depending on the topography (Gantsetseg et al., 2017). The mean annual precipitation during 1975–2019 was 100.4 mm. More than two-thirds of the annual precipitation occurs from June to August. The annual mean temperature was 3.8°C in 2011 with a maximum temperature of 37.1°C in August and a minimum temperature of −31.3°C in January (Ishizuka et al., 2012).

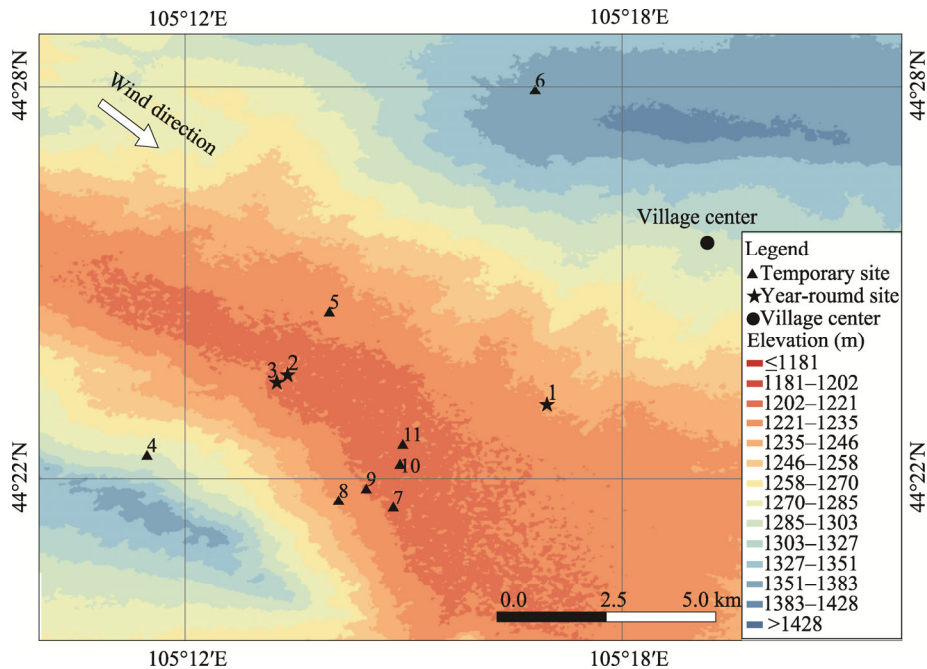


Fig. 1 Topographic map showing the locations of the observation sites around Tsogt-Ovoo. Stars indicate sites where observations were conducted year-round: The Main site (labeled 1; see Table 1) was established in March 2012, and sites Sub14A and Sub14B (labeled 2 and 3, respectively) were established in March 2014. Temporary observation sites are indicated by triangles. Observations were conducted during 1–5 May 2018 at sites Sub18A–Sub18D (labeled 4–7, respectively) and from 27 April to 8 May 2019 at sites Sub19A–Sub19D (labeled 8–11, respectively). Wind speed, wind direction, and sand saltation count were observed at all sites, whereas soil moisture was observed only at the year-round sites.

The sites are located in five different topographic positions, designated southern mountain (S.MT; Sub18A site), southern slope (S.SL; Sub14B, Sub19A, and Sub19B sites), topographic depression (TD; Sub14A, Sub18D, Sub19C, and Sub19D sites), northern slope (N.SL; Main and Sub18B sites), and northern mountain (N.MT; Sub18C site) (Table 1). It should be noted that the two digits in the site name indicate the installation year. We chose the temporary site locations on the basis of land surface features, especially the size and amount of stones.

Figure 2 shows land surface conditions in front of the sand saltation count sensor at the different sites. There was no green or dead vegetation at the Main, Sub14A, and Sub14B sites in spring 2018, but green or dead vegetation was observed at those sites in spring 2019. There was a hard crust at the Sub14A, Sub18A, and Sub18D sites in both years. There was a soft crust on sandy soil at the Sub19C site. Further, at the site Sub19D, there was a sand sheet with no vegetation, crust, or stones.

2.2 Experimental design

Because land surface characteristics differed from site to site in our study area, we compared the simulated threshold friction velocity at each study site with the observed value to validate the theoretical model.

Table 1 Site locations and type, measurement periods, topographic positions, and surface characteristics

No.	Site name	Geographical coordinates		Type of site	Observation period	Topographic position	Surface characteristic
1	Main	44°23'04"N	105°16'59"E	Year-round	1–5 May 2018 27 April–8 May 2019	N.SL	Stone Stone and vegetation
2	Sub14A	44°23'37"N	105°13'24"E	Year-round	1–5 May 2018 27 April–8 May 2019	TD	Hard crust Crust and vegetation
3	Sub14B	44°23'32"N	105°13'12"E	Year-round	1–5 May 2018 27 April–8 May 2019	S.SL	Stone Stone and vegetation
4	Sub18A	44°22'23"N	105°11'28"E	Temporary	1–5 May 2018	S.MT	Stone
5	Sub18B	44°24'26"N	105°14'01"E	Temporary	1–5 May 2018	N.SL	Stone
6	Sub18C	44°27'32"N	105°16'48"E	Temporary	1–5 May 2018	N.MT	Stone
7	Sub18D	44°21'47"N	105°14'51"E	Temporary	1–5 May 2018	TD	Hard crust
8	Sub19A	44°21'52"N	105°14'04"E	Temporary	27 April–8 May 2019	S.SL	Stone
9	Sub19B	44°22'02"N	105°14'27"E	Temporary	27 April–8 May 2019	S.SL	Stone
10	Sub19C	44°22'29"N	105°14'54"E	Temporary	27 April–8 May 2019	TD	Sand and soft crust
11	Sub19D	44°22'39"N	105°14'59"E	Temporary	27 April–8 May 2019	TD	Sand

Note: S.MT, southern mountain; S.SL, southern slope; TD, topographic depression; N.SL, northern slope; N.MT, northern mountain.



Fig. 2 Land surface conditions in front of the saltation count sensor at 14 observation sites. Each site name is shown at the bottom of each photo with the topographic position (MT, mountain; SL, slope; TD, topographic depression) and observation year in parentheses. The diameter of the mouth of the sand catcher was 3.1 cm, and the diameter of the sand saltation count sensor was 1.2 cm.

The workflow for this study is shown in Figure 3. Specifically, image analysis was used to directly measure the height, width, and length of 105 stones at each site; these measurements were used together with the stone coverage to calculate the roughness density of stones. The obtained roughness density was used in a roughness correction parameterization to simulate the threshold friction velocity at each site and to determine the roughness length of the stony sites. The observed wind speed and roughness length were used to calculate the friction velocity. The obtained friction velocity and the observed sand saltation count (hereafter, saltation count) were used to determine the instantaneous threshold friction velocity. The instantaneous threshold values were used to calculate the mean threshold friction velocity during the observation period.

shown in Table 1. Finally, the observed mean was used to validate the simulated threshold friction velocity.

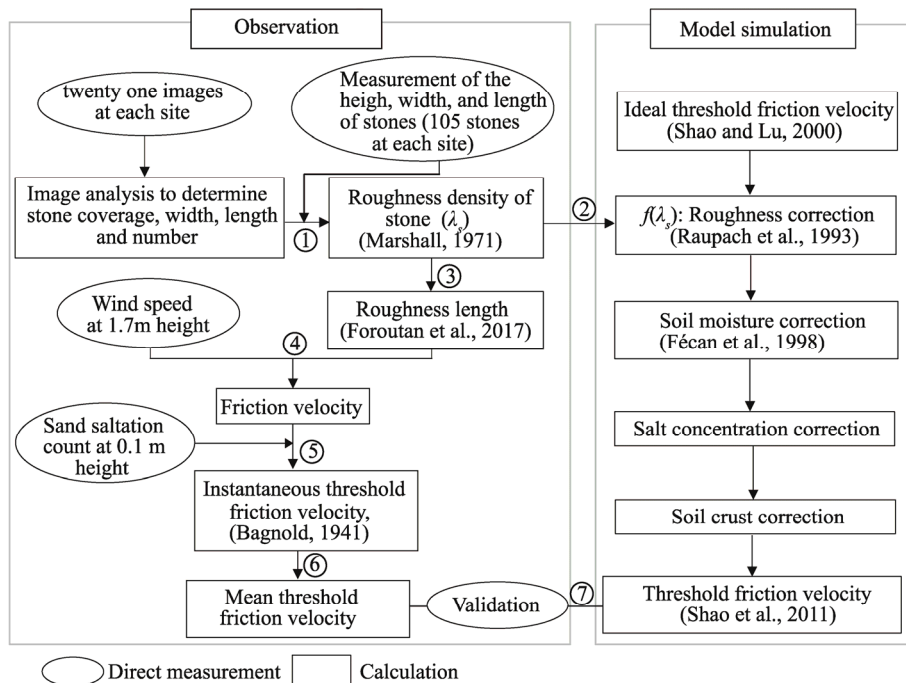


Fig. 3 Workflow showing the observation and model simulation of the threshold friction velocity in this study. λ_s is the roughness density of stones, and $f(\lambda_s)$ is a correction functions for a roughness element.

2.3 Observations of meteorological parameters, saltation count, and soil texture

We measured the spatial coverage and size (i.e., height, width, and length) of stones, meteorological parameters such as wind speed and wind direction, saltation count, and soil texture at each site. Layout of quadrats where land surface photographs were taken for stone measurement and demonstration of anemometer and wind vane are shown in Figure 4. Wind speed, wind direction, and saltation count were measured at each site during 1–5 May 2018 and from 27 April to 8 May, 2019. Anemometers (S-WSA-M003, Onset Company, Bourne, MA, USA) and wind vanes (S-WDA-M003, Onset Company, Bourne, MA, USA) were installed at a height of 1.7 m at each site (Fig. 4b). Saltation count sensors (UD-101, Chuo Kosoku Ltd., Japan) (Udo, 2009) were installed at a height of 0.1 m at each site (Fig. 4b). Soil moisture sensors (S-SMC-M005, Onset Company, Bourne, MA, USA) were installed to 5 cm depth. The saltation count, wind speed, and wind direction were measured at 30 s intervals. The UD-101 sensor was positioned facing the northwest (i.e., 315°), which is the prevailing direction of strong winds in the study area (Ishizuka et al., 2012). We used only the observational data obtained when the wind direction was in the northwest quarter, from 260° to 370° (or 10°). We collected soil samples from the surface layer (1–5 cm depth) at each site and analyzed the soil texture by the dispersion method (Faé et al., 2019). Soil moisture measurements were performed only at the Main, Sub14A, and Sub14B sites.

2.4 Measurements of stones

We used image analysis to obtain the breadth and height of stones and their number for calculating the roughness density of stones at each site. We took 21 photographs of the surface in 30 cm×50 cm quadrats (including the scale) at each site (Fig. 4a). We established three 21-m long observation lines extending northward (N), northwestward (NW), and westward (W) from a point in the southeast part of the site, where the measurement instruments for the saltation count and wind were installed.

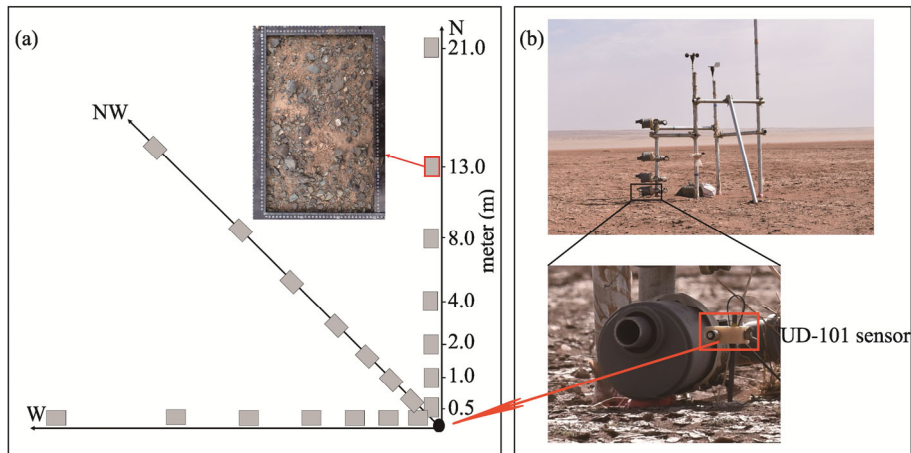


Fig. 4 Layout of quadrats (gray rectangles) where land surface photographs were taken for stone measurement (a) and demonstration of anemometer and wind vane (b). The black dot in the left panel indicates the position of the UD-101 count sensor, which faced northwest. The UD-101 sensor was installed at the height of 0.1 m; the anemometer and wind vane were installed at the height of 1.7 m.

2.4.1 Measurements of stone coverage, width, length, and number by image analysis

We used ImageJ version 1.52p, developed by the U.S. National Institutes of Health to automatically count and measure the number and size of each stone, which are necessary to obtain the roughness density of stones (Mazzoli and Moriconi, 2014). Figure 5 shows the steps involved in image processing.

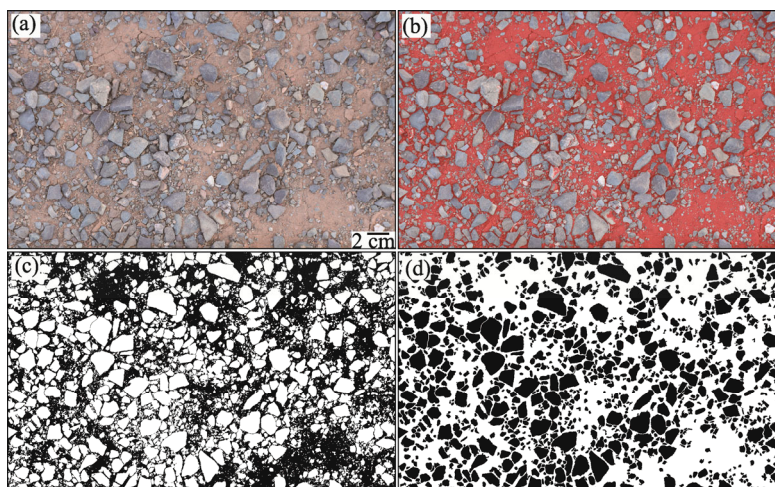


Fig. 5 Demonstration of image processing steps. (a), cropped image with scale; (b), the color threshold for soil that is manually set; (c), image after application of the threshold for stones and the "Fill Holes" and "Watershed" functions to separate particles; (d), final image after application of the "Extended Particle Analyzer" function, which removes coarse sand particles.

In the first step, the pixel size was measured by referring to the 30 cm×50 cm scale (see Fig. 4a). After the scale was set, the image was cropped to exclude the scale (Fig. 5a). In the second step, the "Color Threshold" function was used to color the soil surface, while stones retained their original color. The color threshold was manually adjusted, but we detected some stones on the soil surface with a color similar to that of the soil by tracing their outlines by hand (Fig. 5b). In the third step, we converted the RGB image to an 8-bit grayscale image, setting the soil surface to 0 (black) and the stones to 255 (white). After this step, some gray areas were left. In the fourth step, these gray areas were divided into stone and soil automatically by using the

threshold method of Otsu (1979). However, some fine particles, too small to be stones, were left. Therefore, in the fifth step, the functions "Fill Holes" and "Watershed" were applied to separate these particles (Fig. 5c). Finally, in the sixth step, we revised colors of stones and background and removed fine particles with an area smaller than 0.12 cm^2 , corresponding to a diameter of 4.0 mm, by applying the "Extended Particle Analyzer" function (Fig. 5d). Then, we measured the width, length, and area of each stone and used the stone areas to estimate the stone coverage as the area fraction of stones (black areas in the final image) in each $30 \text{ cm} \times 50 \text{ cm}$ quadrat. The averaged stone coverage of the 21 images was considered to represent the stone coverage at the site.

2.4.2 Roughness density of stones

The roughness density, λ_s (i.e., lateral cover), is defined as the ratio of the total frontal area of all roughness elements to the total surface area, and the calculation formula is as follows:

$$\lambda_s = \frac{ns}{S} = \frac{\sum_{i=1}^n b_i h_i}{S}, \quad (1)$$

where n is the number of roughness elements; b (cm) and h (cm) are the roughness element and height, respectively; s (cm^2) is the mean frontal silhouette area of the obstacles present over the horizontal surface area S (cm^2) (e.g., Marshall, 1971); and i is the stone. The frontal silhouette area of each stone was computed from the width and height of each stone. We determined the breadth of each stone by averaging the width and length of the stone obtained by the image analysis (Section 2.4.1).

We estimated the height of each stone from the two-dimensional image by assuming that the breadth to height ratio at a given site was constant. To obtain the representative breadth to height ratio for each site, we measured the height, width, and length of 105 stones at the site in the field and used the averaged width and length values to calculate the breadth. We calculated the height of each stone in the two-dimensional images using the equation: $h_i = b_i / r$, where r is the representative breadth to height ratio. Finally, we used Equation 1 to calculate roughness density (λ_s). The averaged roughness densities of the 21 images were considered to be the representative roughness density value at each site.

2.5 Roughness length

The aerodynamic roughness length is a function of the mean height, density, and shape of the solid elements. Several studies have empirically determined the relationships among aerodynamic roughness length, roughness mean height, and roughness density of natural desert surfaces, especially sparsely vegetated and stony surfaces (e.g., Lancaster and Baas, 1998; King et al., 2005; Marticorena et al., 2006; Hébrard et al., 2012). Foroutan et al. (2017) compiled aerodynamic roughness length, roughness density, and roughness mean height from data reported by several field and wind tunnel studies (King et al., 2005; Marticorena et al., 2006; Hébrard et al., 2012) and created a comprehensive database of aerodynamic roughness lengths. By fitting straight lines to the relationship between the ratio of aerodynamic roughness length to roughness mean height and roughness density, Foroutan et al. (2017) estimated the aerodynamic roughness length relevant to aeolian processes as follows:

$$\frac{z_0}{h} = \begin{cases} 0.960\lambda_s^{1.07}, & \lambda_s < 0.2 \\ 0.083\lambda_s^{-0.46}, & \lambda_s \geq 0.2 \end{cases} \quad (2)$$

where z_0 (cm) is the aerodynamic roughness length; h (cm) is the roughness mean height; and λ_s is the roughness density.

We used the mean stone height at each site and Equation 2 to determine the aerodynamic roughness length at the stony sites in this study.

For relatively smooth surfaces, aerodynamic roughness length is approximately 1/30 of the mean particle diameter (Greeley and Iversen, 1985). The value of aerodynamic roughness length was used at the sandy sites or sites with crusts (Sub19C, Sub19D and Sub14A).

2.6 Friction velocity and the threshold friction velocity estimated from observations

2.6.1 Friction velocity

The friction velocity, which represents the surface shear stress exerted by the wind, is a critical parameter in numerical dust emission schemes. It determines the onset and end of saltation, and it also affects the horizontal sand flux and the vertical dust flux. By assuming a logarithmic wind profile under neutral conditions, the friction velocity u_* can be calculated as,

$$u_* = \frac{kU_{1.7}}{\log(z/z_0)}, \quad (3)$$

where k is the von Karman constant ($k=0.41$); z_0 (m/s) is the aerodynamic roughness length; z (m) is the observation height ($z=1.7$ m); and $U_{1.7}$ (m/s) is the observed wind speed at the observation height of 1.7 m. Note that in Equation 3, we used the aerodynamic roughness length estimated from the roughness density obtained with Equation 2.

2.6.2 Threshold friction velocity obtained from observations

The threshold friction velocity for sand saltation is commonly defined as the minimum friction velocity required for the initiation of sand transport. Several methods have been employed to calculate this value (Barchyn and Hugenholtz, 2011), although generally the threshold wind velocity is actually calculated instead of the threshold friction velocity. We employed the "Instantaneous Method" of Bagnold (1941), which identifies the friction velocity at which sand saltation begins and ends as the threshold friction velocity (Barchyn and Hugenholtz, 2011). The instantaneous threshold friction velocity ($u_{*t \text{ inst}}$) was estimated every 30 s (Section 2.3), and the mean threshold friction velocity ($u_{*t \text{ mean}}$) over the observation period (Table 1) was used for validating the simulated threshold friction velocities. Figure 6 presents an example of a friction velocity time series to illustrate the method used to determine the instantaneous threshold friction velocities. The black and blue gray lines show the friction velocity when sand saltation was observed or not observed, respectively. The red circles indicate the times at which sand saltation started and ended, and the friction velocities at those times were used as the instantaneous threshold friction velocities. The green line shows the friction velocity when the wind direction was between 10° and 260° . Because the sand saltation sensors (UD-101) faced northwest (i.e., 315°), the instantaneous friction velocities were not determined when the wind direction was between 10° and 260° , although the sand saltation was active.

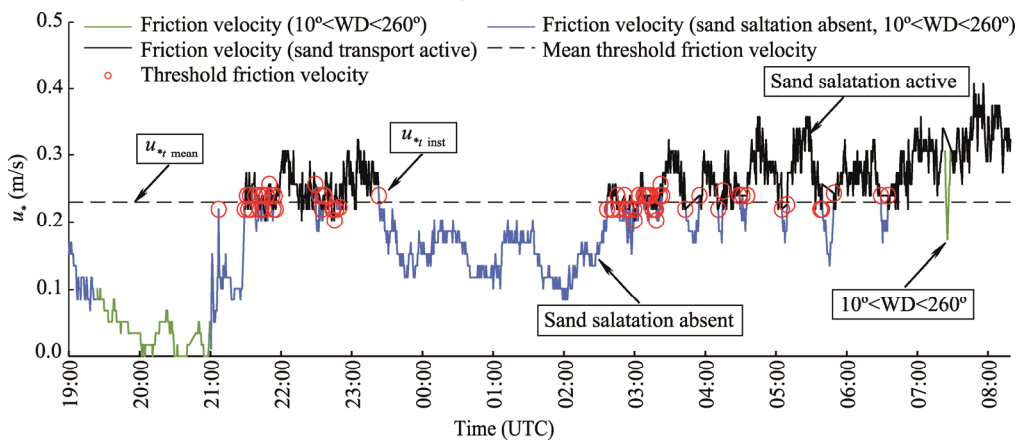


Fig. 6 Time series of friction velocity during 28–29 May 2019 at the site Sub19D. Blue line, no sand transport; black line, active sand transport; $u_{*t \text{ inst}}$, instantaneous threshold friction velocity at the start and end of sand transport; $u_{*t \text{ mean}}$, mean threshold friction velocity (dashed horizontal line). Friction velocities obtained when the wind direction was between 10° and 260° (green line) were not used in the determination of the threshold friction velocity. Friction velocity was calculated using Equation 3 with aerodynamic roughness length of the threshold friction velocity. Friction velocity was calculated using Equation 3 with aerodynamic roughness length of 0.0012 m/s. Wind speed and wind direction (WD) were measured at 1.7 m height. UTC is the Coordinated Universal Time.

2.7 Parameterization of the threshold friction velocity in the numerical model

The threshold friction velocity represents the minimum wind speed for the mobilization of soil grains. Under ideal conditions (i.e., no roughness elements, no soil moisture, no salt concentration, and no soil crust), the threshold friction velocity can be calculated by considering the balance among wind drag, gravity, and interparticle cohesion (Shao and Lu, 2000). The threshold friction velocity (u_{*t}) for an arbitrary surface that is affected by roughness elements (shear stress partitioning), soil moisture, salt concentration, and soil crust is expressed as follows:

$$u_{*t} = (d_s, \lambda, w, s_c, s_{cr}) = u_{*t0}(d_s) f(\lambda) f(w) f(s_c) f(s_{cr}), \quad (4)$$

where d_s (mm) is the sand particle size; u_{*t0} (m/s) is the threshold friction velocity of sand particles of size under ideal conditions; λ , w (m^3/m^3), s_c , and s_{cr} are the roughness density of the roughness elements, soil moisture, salt concentration, and soil crust, respectively; and $f(\lambda)$, $f(w)$, $f(s_c)$, and $f(s_{cr})$ are the correction functions for surface roughness elements, soil moisture, salt concentration, and soil crust, respectively (Shao et al., 2011). All of these correction functions are equal to or greater than 1. $f(s_c)$ and $f(s_{cr})$ are often set to 1 in numerical simulations because of the lack of parameterizations and data. Shao and Lu (2000) derived the following simple expression for an ideal threshold friction velocity:

$$u_{*t0}(d_s) = \sqrt{A_N \left(\frac{\rho_p}{\rho_a} g d_s + \frac{A_L}{\rho_a d_s} \right)}, \quad (5)$$

where ρ_p (kg/m^3) is the sand particle density ($\rho_p = 2560 \text{ kg}/\text{m}^3$); ρ_a (kg/m^3) is the air density ($\rho_a = 1.225 \text{ kg}/\text{m}^3$); g (m/s^2) is the gravitational acceleration ($g = 9.81 \text{ m}/\text{s}^2$); and A_N and A_L are constants ($A_N = 0.0123$ and $A_L = 1.65 \times 10^{-4} \text{ kg}/\text{s}^2$), which account for the magnitude of the interparticle cohesive forces and are empirically determined by a wind tunnel experiment (Greeley and Iversen, 1985). Note that we did not measure the sand particle size d_s at the observation sites. In this study, we used the minimum values of the threshold friction velocity of sand particles of size corresponding to a soil particle diameter of about 80 μm .

2.7.1 Surface roughness effect (shear stress partitioning effect)

We adapted the surface roughness factor of Raupach et al. (1993) based on drag partitioning to include the effects of solid elements (i.e., stones):

$$f(\lambda) = \sqrt{(1 - \sigma_s m_s \lambda_s)(1 + \beta_s m_s \lambda_s)}, \quad (6)$$

$$\beta_s = \frac{C_R}{C_s}, \quad (7)$$

where σ_s is the ratio of the basal to frontal area of the roughness elements; m_s is a parameter accounting for spatial nonuniformity of surface stress that ranges between 0 and 1 (1 for uniform stress and decreasing as nonuniformity increases); λ_s is the roughness density of the solid elements (Raupach et al., 1993); β_s is representing the drag partition of a single roughness element; C_R is the drag coefficient for isolated roughness elements; and C_s is the drag coefficient for the soil surface. In this study, we used the average roughness density of stones at each site for representing the roughness density of the solid elements. For β_s , Shao et al. (2015) recommended using a value between 100 and 400. In this study, following Tan et al. (2019), we set $m_s = 0.5$ and $\beta_s = 100$. For obtaining the σ_s , we used the measured values at each site (i.e., the average ratio of breadth to height of the 105 stones). We assumed that σ_s was constant at a given site.

2.7.2 Effects of soil moisture, salt concentration, and soil crust

Fécan et al. (1998) parameterized the influence of soil moisture as a function of the clay content by fitting an equation to the experimental data for various soils. Shao and Lu (2000) used observational data to expand the parameterization of Fécan et al. (1998) for several soil textures and obtained the following equation:

$$f(w) = \begin{cases} 1 & \text{for } w < w_r \\ \frac{1}{\sqrt{1 + a(w - w_r)^b}} & \text{for } w \geq w_r \end{cases}, \quad (8)$$

where w (m^3/m^3) is the volumetric soil moisture; a and b are parameters that depend on soil texture; and w_r (m^3/m^3) is the threshold soil moisture value, which depends on the soil texture (Kang et al., 2011). Our measured soil moisture during the observational periods was always lower than the threshold value. Therefore, we set $f(w)=1$ in the simulation. We found no salt accumulation in the study area, so we did not measure salt concentration and set $f(s_c)=1$. A soil crust was sometimes present (Table 1), but we had no method for measuring its hardness. Thus, we also set $f(s_{cr})=1$.

3 Results

3.1 Roughness density and roughness length

Table 2 shows the measurement results for soil texture and the parameters for stones (coverage, mean stone height, roughness density, and roughness length) at all sites. The soil texture at all sites was loam, except for sandy loam and silt loam at the sites Sub18C and Sub18D, respectively. The three highest stone coverages were 57.1% at the Sub18A site (S.MT; Table 1), 47.2% at the Sub19A site (S.SL), and 39.7% at the Sub19B site (S.SL). The next highest coverages were 33.9% at the Sub18C site (N.MT), 28.8% at the Sub18B site (N.SL), 22.4% at the Sub14B site (S.SL), and 18.6% at the Main site (N.SL). The stone coverage was only 2.9% at the Sub18D site (TD) and 0.0% at the Sub14A (TD), Sub19C (TD), and Sub19D (TD) sites. Mean stone height, roughness density, and roughness length generally tended to increase with increasing stone coverage.

We examined the relationship between stone coverage and roughness density based on the data of this study and based on the data reported by Marticorena et al. (2006) (Fig. 7); we fitted a third-degree polynomial to the data. The roughness density increased gradually when the stone coverage was from 0.0% to 30.0%; it increased relatively quickly between coverages of 30.0% and 50.0% and apparently increased gradually again when stone coverage exceeded 50.0%. This result suggests that it may be possible to estimate the roughness density of stones from the stone coverage. At the sites Sub18A, Sub19A, Sub19B, Sub18C, Sub18B, Sub14B, Main, and Sub18D, the frequency distribution of the ratio of breadth to height was normal (Fig. 8).

Table 2 Measurement results for coverage, mean height, roughness density, and roughness length of stones at each site

Site name	Soil texture	Stone coverage (%)		Ratio of breadth to height		Height (cm)		Roughness density		Roughness length (cm)
		Mean	SD	Mean	SD	Mean	SD	Mean	SD	
Main	Loam	18.6	2.95	1.75	0.37	0.39	0.15	0.05	0.001	0.0152
Sub14A	Loam	0.0	–	–	–	–	–	0.00	–	0.0012
Sub14B	Loam	22.4	3.52	1.81	0.30	0.57	0.23	0.07	0.016	0.0318
Sub18A	Loam	57.1	5.84	1.88	0.36	1.05	0.27	0.34	0.039	0.1569
Sub18B	Loam	28.8	3.26	1.85	0.35	0.48	0.19	0.13	0.017	0.0519
Sub18C	Sandy Loam	33.9	4.25	1.74	0.43	0.65	0.37	0.16	0.023	0.0878
Sub18D	Silt Loam	2.9	1.01	1.93	0.41	0.47	0.16	0.01	0.004	0.0011
Sub19A	Loam	47.2	4.13	1.89	0.37	1.01	0.35	0.32	0.031	0.1587
Sub19B	Loam	39.7	4.73	1.84	0.39	0.89	0.30	0.24	0.036	0.1628
Sub19C	Loam	0.0	–	–	–	–	–	0.00	–	0.0012
Sub19D	Loam	0.0	–	–	–	–	–	0.00	–	0.0012

Note: SD, standard deviation; –, no data available.

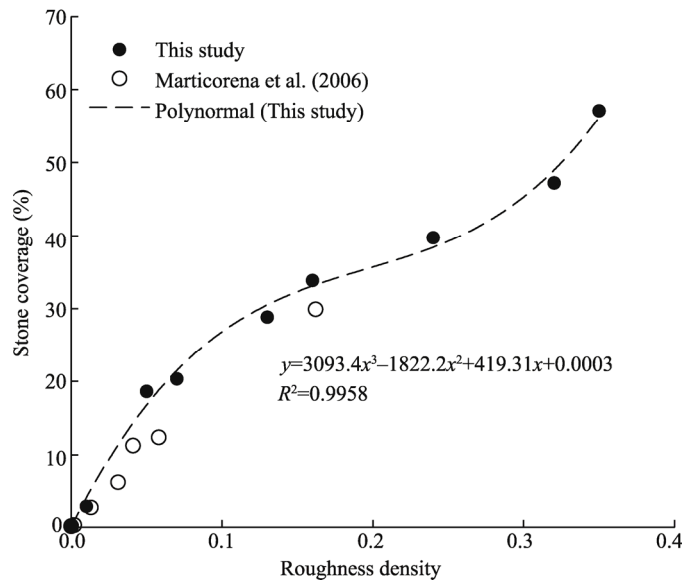


Fig. 7 Relationship between stone coverage and roughness density from this study (black dots) and the study of Marticorena et al. (2006) (open circles)

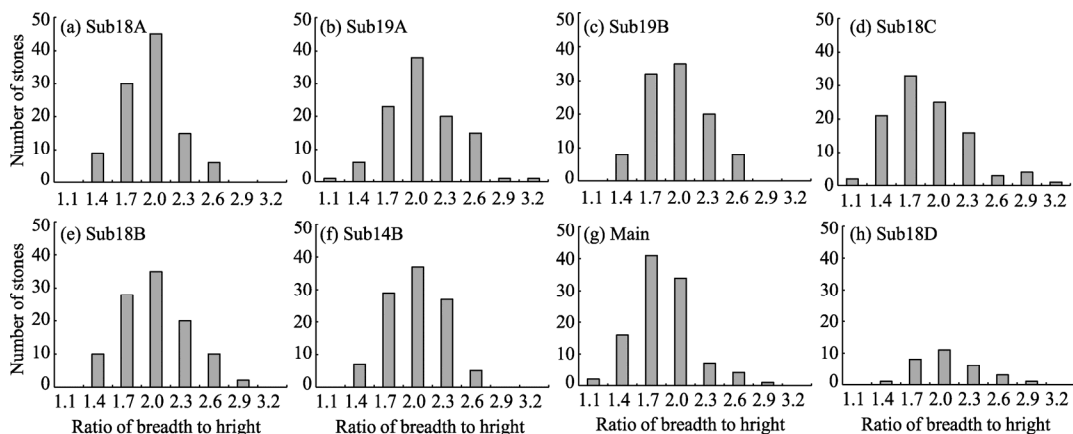


Fig. 8 Frequency distributions of the ratio of breadth to height of stones at the sites Sub18A (a), Sub19A (b), Sub19B (c), Sub18C (d), Sub18B (e), Sub14B (f), Main (g), and Sub18D (h)

Although the coverage, mean height, and roughness density differed greatly from site to site, the mean ratio was similar among the sites (Table 2). The roughness correction is related to the ratio of breadth to height (i.e., the ratio of the basal to frontal area of the roughness elements (σ_s) in Eq. 6); thus, it is possible to use the observed mean ratio in the model simulation because the ratio is normally distributed. Previous dust model studies that considered the effect of stones on the threshold friction velocity have used a value of 1.00 for this ratio, but in this study, the average ratio was 1.84.

3.2 Observed threshold friction velocity and the effects of roughness density

Figures 9 and 10 show the time series of friction velocity (green and blue lines), the instantaneous threshold friction velocities (red circles), and their temporal means (dashed lines) at the sites during 1–5 May 2018 and 27 April–8 May 2019, respectively. Sand saltation was observed at all sites in 2019 and at three sites in 2018, but almost no saltation was observed at the other four sites in 2018.

Under the natural field conditions, the instantaneous friction threshold at the sites was not constant. However, during both measurement periods, the temporal difference was much smaller

than the difference in the mean threshold among the sites. The standard deviation of the instantaneous threshold friction velocity around the mean threshold friction velocity value at each site was between 0.03 and 0.07 m/s, whereas the standard deviation around the average of the mean threshold friction velocity among the sites was 0.15 m/s. The highest mean threshold friction velocity (0.71 m/s) was recorded at the site Sub19A, where the roughness density was highest (0.320) in 2019. The lowest mean threshold friction velocity (0.23 m/s) was recorded at the site Sub19D, where no stones were observed in 2019.

We examined the relationship between roughness density and mean threshold friction velocity at seven sites in 2019 and three sites in 2018 (Fig. 11). Observations were also conducted at the sites Sub14A, Sub18A, Sub18B, and Sub18D in 2018, but we could not obtain the threshold friction velocity because saltation counts were too few. The mean threshold friction velocity tended to increase with increasing roughness density. We divided the dataset into three groups according to roughness density: Group 1 consisted of 2019Sub14A, 2019Sub19C, and 2019Sub19D sites (roughness density=0.000); Group 2 consisted of 2018Main and 2019Main (roughness density=0.050); and Group 3 consisted of 2018Sub14B and 2019Sub14B (roughness density=0.070). The four digits before the site name indicate the year of observation.

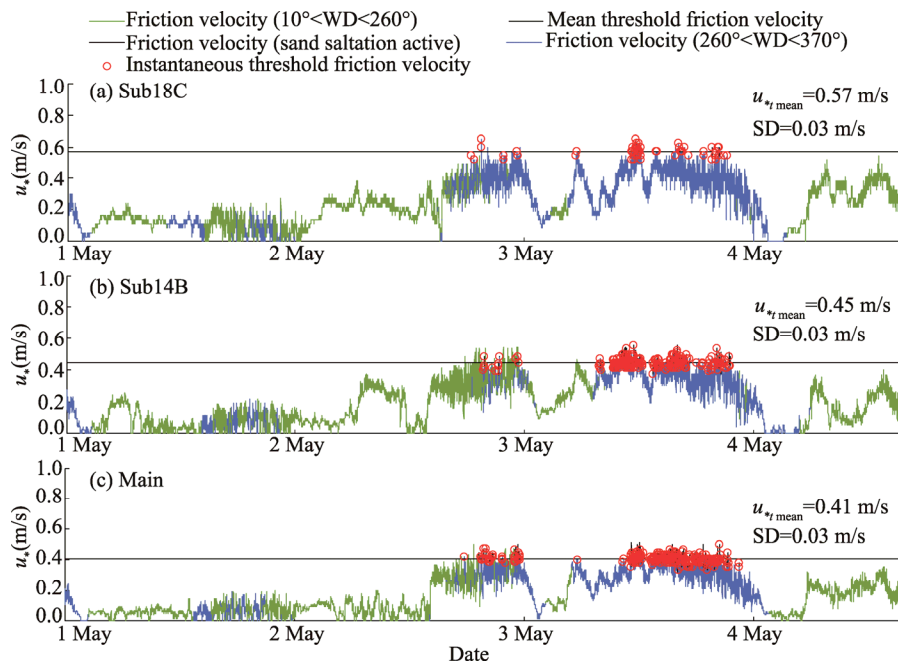


Fig. 9 Friction velocity when the wind direction was between 260° and 370° (i.e., 10°) (blue lines) or between 10° and 260° (green lines), instantaneous threshold friction velocity (red circles), and mean threshold friction velocity (dashed lines) during 1–5 May 2018 at the sites Sub18C (a), Sub14B (b), and Main (c). $u_{*f,mean}$, mean threshold friction velocity; SD, standard deviation of the instantaneous thresholds around the mean.

3.3 Simulated threshold friction velocity and validation against observations

Figure 12 shows the relationship between the observed threshold friction velocity and simulated threshold friction velocity by using the measured roughness density of stones at each site. The simulated threshold friction velocity was the same within each of the three groups: Group 3, 0.42 m/s; Group 2, 0.37 m/s; and Group 1, 0.20 m/s. These values corresponded to roughness densities of 0.070, 0.050, and 0.000, respectively. The observed and simulated threshold friction velocities were almost the same at the sandy site Sub19D and at the stony sites 2018Sub14B, 2018Main, Sub18C, Sub19A, and Sub19B (see Table 1), but the simulated threshold friction velocities for the sites in groups 1–3 tended to be substantially underestimated.

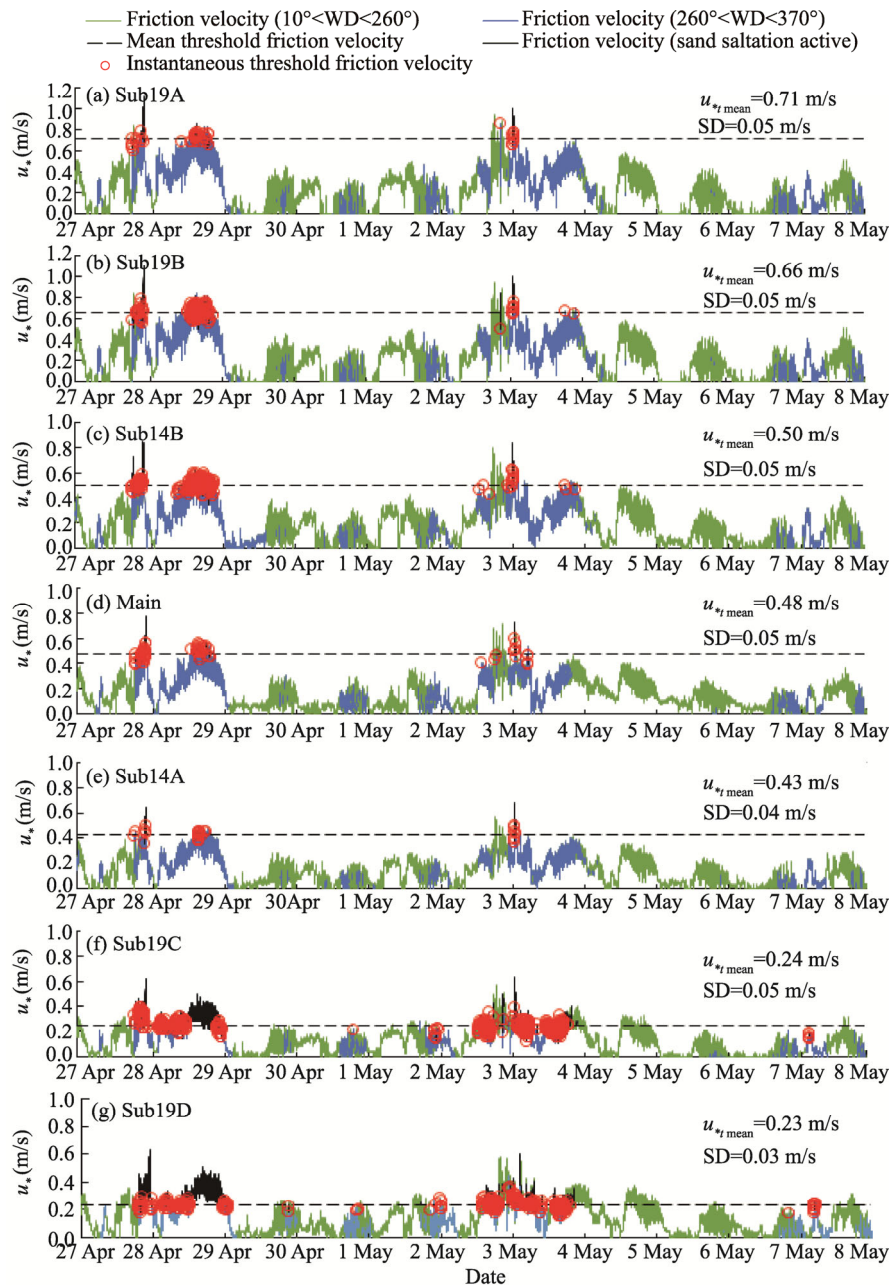


Fig. 10 Friction velocity when the wind direction was between 260° and 370° (i.e., 10°) (blue lines) or between 10° and 260° (green lines), instantaneous threshold friction velocity (red circles), and mean threshold friction velocity (dashed lines) from 27 April to 8 May 2019 at the sites Sub19A (a), Sub19B (b), Sub14B (c), Main (d), Sub14A (e), Sub19C (f), and Sub19D (g).

4 Discussion

4.1 Soil texture, stone coverage, topography, and dust source

We found no relationship between the spatial distribution of soil texture and topography, but parameters of stones such as coverage and roughness density tended to increase from lowland (i.e., TD) to highland (i.e., MT) sites. In addition, those parameters tended to be higher at the southern sites (i.e., S.MT and S.SL) than at the northern sites (i.e., N.MT and N.SL), which

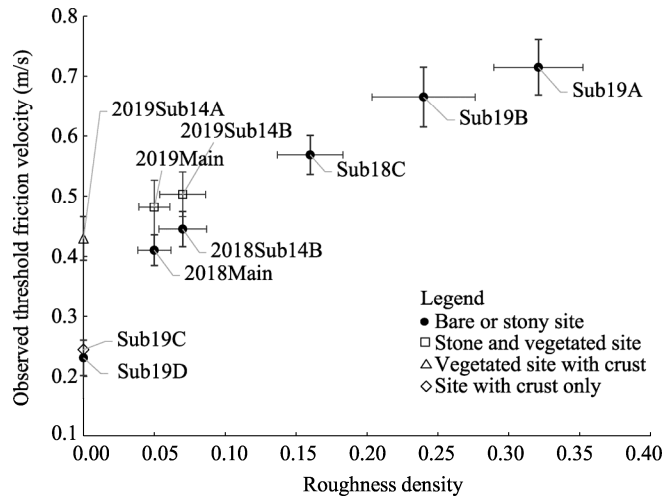


Fig. 11 Relationship between roughness density and mean threshold friction velocity observed at the bare or stony (i.e., no vegetation and no crust) sites (black dots), stony and vegetated sites (open rectangles), vegetated site with crust (open triangle), and site with crust only (open rhombus) in spring 2018 and 2019. Symbols show the average roughness density and mean observed threshold friction velocity, and bars show their standard deviations. For sites Main, Sub14A, and Sub14B, where observations were carried out year-round, the four digits before the site name indicate the year of the observations.

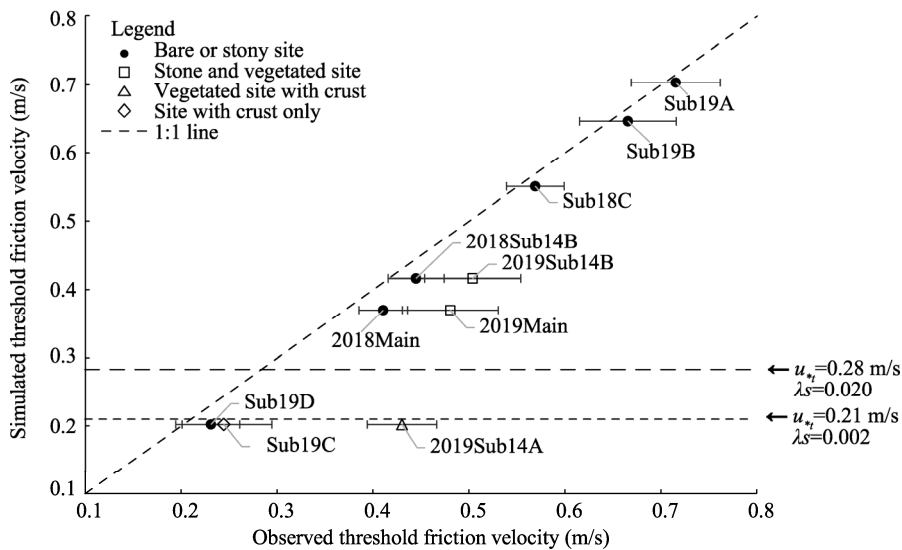


Fig. 12 Scatter plot between the observed threshold friction velocity (during 1–5 May 2018 and during 27 April–8 May 2019) and simulated threshold friction velocity using the observed roughness density of stones at the bare or stony (i.e., no vegetation and no crust) sites (black dots), stony and vegetated sites (open rectangles), vegetated site with crust (open triangle), and site with crust only (open rhombus). The two horizontal thin dashed lines show the simulated threshold friction velocity using roughness densities of 0.002 and 0.020 for barren and sparsely vegetated land cover types, respectively.

resulted in the threshold friction velocities being low in lowlands and high in highlands. Our results agreed with the findings of Callot et al. (2000), who revealed that the size of non-erodible elements such as stones was dependent on the distance from the highest topographic point.

It is well known that dust sources are often distributed in topographic lows and lands adjoining topographic highs (e.g., Shao, 2008); in this study, such areas are represented by the TD sites. Our findings that areas with almost no stone coverage were associated with low threshold friction velocities are consistent with this well-known observation about dust sources.

4.2 Effects of other factors on threshold friction velocity than stones

We found that sites with the same roughness density (Figs. 11 and 12) can have different observed threshold friction velocities. The roughness density of stones was 0.070 at the sites 2018Sub14B and 2019Sub14B (Group 3), 0.050 at the sites 2018Main and 2019Main (Group 2), and 0.000 at the sites 2019Sub14A, Sub19C, and Sub 19D (Group 1). Increased soil moisture and salt accumulation can increase the threshold friction velocity. However, during our observation periods, the observed soil moisture was very low (less than $0.05 \text{ m}^3/\text{m}^3$), though it was observed at the sites Main, Sub14B, and Sub14A only; further, no salt accumulation was observed.

In 2019, dead vegetation was observed at the sites Main, Sub14B, and Sub14A, and green vegetation was observed at the site Sub14A, whereas no vegetation was observed at these sites in 2018 (Fig. 13). Many studies have shown that vegetation reduces wind erosion intensity through coverage and shear stress partitioning effects, which decrease soil erodibility, and as a result, the sand saltation threshold increases (e.g., Lancaster and Baas, 1998; Li et al., 2008; Yan et al., 2011). We can infer that the presence of herbaceous vegetation (live or dead) led to higher threshold friction velocities at the sites Main and Sub14B in spring 2019.

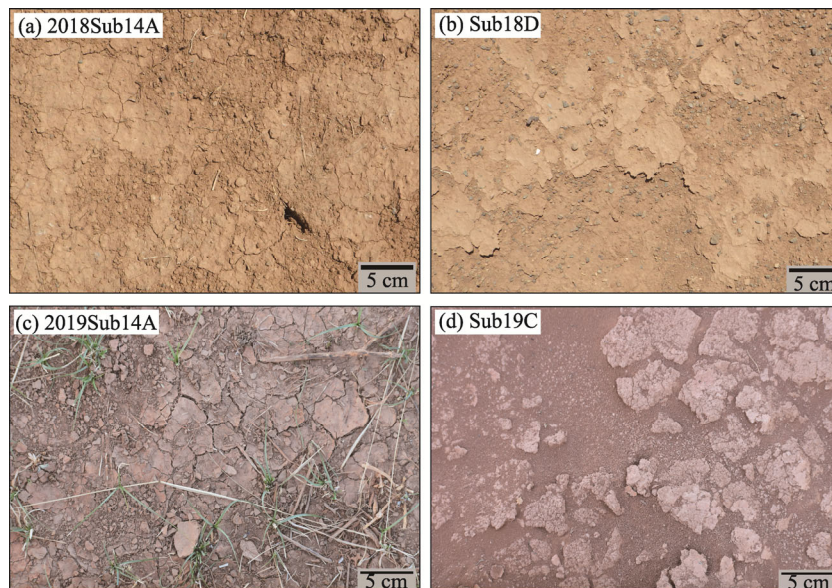


Fig. 13 Crust conditions at the sites Sub14A (a) and Sub18D (b) in spring 2018, and at the sites Sub14A (c) and Sub19C (d) in spring 2019

In the field, the effects of stones and vegetation on wind erosion cannot be separated from those of other factors, such as changes in soil properties or the presence of a crust (Lopez et al., 1998). We observed crust at the sites Sub14A and Sub18D in 2018 and at the sites Sub14A and Sub19C in 2019 (Fig. 13), but the characteristics of the crust differed among the sites. In 2018, the observed crust was mostly undisturbed and sand particles were less mobile at the sites Sub14A and Sub18D. In 2019, the area of disturbed crust was larger at the site Sub14A, but some less-mobile sand particles were still seen, and at the site Sub19C, although a crust was observed, many mobile sand particles were present.

It is very difficult to quantitatively estimate the threshold friction velocity under crusted conditions because many factors, including its morphological and compositional properties (i.e., the modulus of rupture, thickness, and clay, calcium carbonate, water soluble material, and organic matter contents), need to be taken into account (Gillette et al., 1982). However, a well-developed crust can protect soil surfaces, thereby reducing wind erosion intensity (Belnap and Gillette, 1998). Marticorena et al. (1997a) showed that the threshold friction velocity was much higher when crust was undisturbed than when it was disturbed.

Crust was observed at the sites 2019Sub14A and Sub19C (Fig. 13). In the plot of the simulated threshold friction velocity against the observed threshold friction velocity (Fig. 12), the site 2019Sub14A was far to the right of the 1:1 line, indicating that the observed threshold friction velocity was much higher than the simulated threshold friction velocity based on the observed roughness density of stones alone. Because the site has vegetation as well as crust, we cannot isolate the effect of the crust alone, but this result demonstrates that vegetation and crust both increase the threshold friction velocity.

The site Sub19C was also located on the right of the 1:1 line in Figure 12. In addition, the observed threshold friction velocity was slightly higher at the site Sub19C than at the site Sub19D. The crust may have caused the threshold friction velocity to be higher at the site Sub19C than at the site Sub19D. However, these sites may be located nearer the 1:1 line because of sand particle mobility; many mobile sand particles were observed at the sites Sub19C and Sub19D and were relatively fewer at all other sites.

As discussed in Section 4.1, the topographic depression may be a major dust source because stones are almost completely absent there. However, vegetation and crust were distributed mostly in the topographic depression (Table 1). Gantsetseg et al. (2017) reported that the Normalized Difference Vegetation Index (NDVI) was high in the topographic depression in Tsogt-Ovoo during the rainy summer of 2012. Their result supports our finding of dead vegetation mainly in the topographic depression in spring because dead vegetation represents vegetation that grew in the previous summer or earlier. We could not quantitatively examine the effects of vegetation and crust on the threshold friction velocity due to a lack of data, but we could determine that an increase in the threshold friction velocity was resulted from their effects. In addition, the gaps in the observed threshold friction velocities between sites Sub19D and 2019Sub14A, between sites 2018Main and 2019Main, and between sites 2018Sub14B and 2019Sub14B quantitatively implied the importance of vegetation and crust at these sites.

4.3 Effects of stones on the threshold friction velocity in the three-dimensional model studies

It is currently difficult to account for the effects of stones on the threshold friction velocity in a three-dimensional dust model because no reliable data on the spatial distribution of stones are available. However, several studies (e.g., Darnenova et al., 2009; Xi and Sokolik, 2015; Foroutan et al., 2017; Lee and Park, 2020) have conducted a three-dimensional dust simulation by employing a double shear stress partition scheme. These studies prepared a lookup table that contains representative roughness density values of solid elements (i.e., stones) and vegetation for each land cover type. The studies used roughness density values of 0.002 (Darnenova et al., 2009; Foroutan et al., 2017) and 0.020 (Xi and Sokolik, 2015; Lee and Park, 2020) for barren and sparsely vegetated land cover types, respectively. In this study, all of the sites were considered barren or sparsely vegetated, the threshold friction velocity simulated with roughness density of 0.002 was 0.21 m/s, and that simulated with roughness density of 0.020 was 0.28 m/s (horizontal dashed lines in Fig. 12). Even though all of the sites in this study were classified as barren or sparsely vegetated, our results showed that the threshold friction velocities simulated using with the observed roughness density varied from 0.20 m/s at the bare sites in the topographic depression, to 0.70 m/s at the stony sites on the southern mountain with roughness density of 0.000; and these simulated threshold friction velocities were almost the same as those observed values at the sites with roughness density of 0.320.

When we compared the threshold friction velocity estimated by the three-dimensional dust models employing a constant roughness density with threshold friction velocities estimated for bare or stony sites (black dots in Fig. 12), we found that the threshold friction velocity estimated by the three-dimensional dust models employing roughness density of 0.002 was almost same as that at a sandy site (Sub19D) in the topographic depression, but the three-dimensional dust models employing roughness density of 0.020 overestimated the threshold friction velocity at that site. Moreover, the three-dimensional dust models employing both roughness density values of 0.002 and 0.020 consistently underestimated the threshold friction velocity at the sites on

slopes and mountains (e.g., 2018Main, 2018Sub14B, Sub18C, Sub19B, and Sub19A). Our survey result showing that the roughness density varies over a wide range even among sites with the same land cover type suggests that reliable spatial distribution data of stones based on field measurements are necessary to achieve realistic three-dimensional dust simulation results.

We expect it to be possible to obtain spatial distribution data of stones over a wide area by satellite remote sensing techniques. Some studies have already estimated roughness parameters from satellite data. Greeley et al. (1991) found an empirical correlation between the aerodynamic roughness length of non-erodible elements and the radar backscatter coefficient obtained by Airborne Synthetic Aperture Radar (AIRSAR), and Marticorena et al. (2004) obtained a good relation between the aerodynamic roughness length and the Polarization and Directionality of the Earth's Reflectance (POLDER)-1 bidirectional reflectance distribution function (BRDF).

Laurent et al. (2005) conducted a three-dimensional dust simulation using a roughness length map obtained by the BRDF method of Marticorena et al. (2004), but the mapped data comprise roughness values due to both stones and vegetation. For a simulation that discriminates the effects of stones and vegetation, such as a simulation using a double shear stress partition scheme, satellite observation techniques that can separately quantify stones and vegetation are needed.

5 Conclusions

We evaluated the effects of stones on the sand saltation threshold for different roughness densities of stones by conducting field observations under natural surface conditions during sand and dust storms in the northern part of the Gobi Desert, Mongolia. We found that sand saltation threshold noticeably increased with the increasing roughness density of stones. Specifically, roughness density increased from lowland to highland sites. At the sites to the north of Tsogt-Ovoo, where neither crust nor vegetation was observed, the roughness density values were 0.000, 0.050, and 0.160 at the TD, N.SL and N.MT sites, respectively. To the south, the values were 0.000 and 0.070–0.320 at the TD and S.SL sites, respectively. The stone coverage also increased from lowland to highland sites; at the sites to the north, where neither crust nor vegetation was observed, the mean threshold friction velocities (the average of the instantaneous threshold friction velocities) were 0.23, 0.41, and 0.57 m/s at the TD, N.SL, and N.MT sites, respectively. To the south, they were 0.23 and 0.45–0.71 m/s at the TD and N.SL sites, respectively.

We simulated the threshold friction velocity with the model, which includes the Raupach's roughness correction that uses measured roughness density values. We found that this roughness correction worked very well in the study area. The threshold friction velocity was simulated very well at all sites where neither crust nor vegetation was observed, although the simulated threshold friction velocity showed a small negative bias. Though our survey was conducted in only one small area in the vast Gobi Desert, our results suggest that if roughness density of stones over a wide area can be obtained, the roughness correction for the stone effect in the model of roughness correction can be applied in the three-dimensional dust models. The simulation results of this study also showed that, to reasonably simulate sand saltation in the Gobi Desert, it is essential to consider the effects of vegetation and crust as well as the effects of stones.

Acknowledgements

This study was supported by the Arid Land Research Center's Project (Impacts of Climate Change on Drylands: Assessment and Adaptation, funded by the Japan's Ministry of Education, Culture, Sports, Science, and Technology), the Grants-in-Aid for Scientific Research (JSPS KAKENHI) (15H05115, 17H01616, 16H02712, and 25220201), and the Environment Research and Technology Development Fund of the Environmental

Restoration and Conservation Agency (JPMEERF20205001). This study was funded by the Joint Research Program of Arid Land Research Center, Tottori University (31C2003 and 31C2012).

References

- Bagnold R A. 1941. The physics of blown sand and desert dunes. *Progress in Physical Geography*, 18(1): 91–96.
- Barchyn T E, Hugenholtz C H. 2011. Comparison of four methods to calculate aeolian sediment transport threshold from field data: Implications for transport prediction and discussion of method evolution. *Geomorphology*, 129(3–4): 190–203.
- Belnap J, Gillette D A. 1998. Vulnerability of desert biological soil crusts to wind erosion: the influences of crust development, soil texture, and disturbance. *Journal of Arid Environments*, 39(2): 133–142.
- Boucher O, Randall D, Artaxo P, et al. 2013. Clouds and aerosols. In: *Climate Change 2013: The Physical Science Basis. Contribution of Working Group I to the Fifth Assessment Report of the Intergovernmental Panel on Climate Change*. Cambridge: Cambridge University Press, 571–657.
- Callot Y, Marticorena B, Bergametti G. 2000. Geomorphologic approach for modelling the surface features of arid environments in a model of dust emissions: application to the Sahara Desert. *Geodinamica Acta*, 13(5): 245–270.
- Chen S, Huang J, Li J, et al. 2017. Comparison of dust emissions, transport, and deposition between the Taklimakan Desert and Gobi Desert from 2007 to 2011. *Science China Earth Sciences*, 60(7): 1338–1355.
- Cooke R U. 1970. Stone pavements in deserts. *Annals of the Association of American Geographers*, 60(3): 560–577.
- Darmenova K, Sokolik I N, Shao Y, et al. 2009. Development of a physically based dust emission module within the Weather Research and Forecasting (WRF) model: Assessment of dust emission parameterizations and input parameters for source regions in Central and East Asia. *Journal of Geophysical Research: Atmospheres*, 114(D14), doi: 10.1029/2008JD011236.
- Edwards B L, Namikas S L. 2015. Characterizing the sediment bed in terms of resistance to motion: Toward an improved model of saltation thresholds for aeolian transport. *Aeolian Research*, 19: 123–128.
- Faé G S, Montes F, Bazilevskaya E, et al. 2019. Making soil particle size analysis by laser diffraction compatible with standard soil texture determination methods. *Soil Science Society of America Journal*, 83(4): 1244–1252.
- Fécan F, Marticorena B, Bergametti G. 1998. Parametrization of the increase of the aeolian erosion threshold wind friction velocity due to soil moisture for arid and semi-arid areas. *Annales Geophysicae*, 17: 149–157.
- Foroutan H, Young J, Napelenok S, et al. 2017. Development and evaluation of a physics-based windblown dust emission scheme implemented in the CMAQ modeling system. *Journal of Advances in Modeling Earth Systems*, 9(1): 585–608.
- Gantsetseg B, Ishizuka M, Kurosaki Y, et al. 2017. Topographical and hydrological effects on meso-scale vegetation in desert steppe, Mongolia. *Journal of Arid Land*, 9(1): 132–142.
- Gillette D A. 1978. Tests with a portable wind tunnel for determining wind erosion threshold velocities. *Atmospheric Environment*, 12(12): 2309–2313.
- Gillette D A, Adams J, Endo A, et al. 1980. Threshold velocities for input of soil particles into the air by desert soils. *Journal of Geophysical Research: Oceans*, 85(C10): 5621–5630.
- Gillette D A, Adams J, Muhs D, et al. 1982. Threshold friction velocities and rupture moduli for crusted desert soils for the input of soil particles into the air. *Journal of Geophysical Research: Oceans*, 87(C11): 9003–9015.
- Gillette D A. 1988. Threshold friction velocities for dust production for agricultural soils. *Journal of Geophysical Research: Atmospheres*, 93(D10): 12645–12662.
- Gillette D A, Herrick J E, Herbert G A. 2006. Wind characteristics of mesquite streets in the northern Chihuahuan Desert, New Mexico, USA. *Environmental Fluid Mechanics*, 6(3): 241–275.
- Gillies J A, Lancaster N, Nickling W G, et al. 2000. Field determination of drag forces and shear stress partitioning effects for a desert shrub (*Sarcobatus vermiculatus*, greasewood). *Journal of Geophysical Research: Atmospheres*, 105(D20): 24871–24880.
- Gillies J A, Nickling W G, King J. 2007. Shear stress partitioning in large patches of roughness in the atmospheric inertial sublayer. *Boundary-Layer Meteorology*, 122(2): 367–396.
- Greeley R, Iversen J D. 1985. *Wind as a geological process on Earth, Mars, Venus and Titan*. Cambridge: Cambridge University Press, 333.
- Greeley R, Gaddis L, Lancaster N, et al. 1991. Assessment of aerodynamic roughness via airborne radar observations. In: *Aeolian Grain Transport*. Vienna: Springer, 77–88.
- Hébrard E, Listowski C, Coll P, et al. 2012. An aerodynamic roughness length map derived from extended Martian rock abundance data. *Journal of Geophysical Research: Planets*, 117(E4), doi: 10.1029/2011JE003942.
- Ishizuka M, Mikami M, Yamada Y, et al. 2009. Threshold friction velocities of saltation sand particles for different soil

- moisture conditions in the Taklimakan Desert. *Sola*, 5: 184–187.
- Ishizuka M, Mikami M, Yamada Y, et al. 2012. Does ground surface soil aggregation affect transition of the wind speed threshold for saltation and dust emission? *SOLA*, 8: 129–132.
- Iversen J D, Wang W P, Rasmussen K R, et al. 1990. The effect of a roughness element on local saltation transport. *Journal of Wind Engineering and Industrial Aerodynamics*, 36: 845–854.
- Kang J Y, Yoon S C, Shao Y, et al. 2011. Comparison of vertical dust flux by implementing three dust emission schemes in WRF/Chem. *Journal of Geophysical Research: Atmospheres*, 116(D9), doi: 10.1029/2010JD014649.
- King J, Nickling W G, Gillies J A. 2005. Representation of vegetation and other nonerodible elements in aeolian shear stress partitioning models for predicting transport threshold. *Journal of Geophysical Research: Earth Surface*, 110(F4), doi: 10.1029/2004JF000281.
- Kurosaki Y, Mikami M. 2007. Threshold wind speed for dust emission in East Asia and its seasonal variations. *Journal of Geophysical Research: Atmospheres*, 112(D17), doi: 10.1029/2006JD007988.
- Kurosaki Y, Shinoda M, Mikami M. 2011a. What caused a recent increase in dust outbreaks over East Asia? *Geophysical Research Letters*, 38(11), doi: 10.1029/2011GL047494.
- Kurosaki Y, Shinoda M, Mikami M, et al. 2011b. Effects of soil and land surface conditions in summer on dust outbreaks in the following Spring in a Mongolian Grassland. *SOLA*, 7: 69–72.
- Lancaster N, Baas A. 1998. Influence of vegetation cover on sand transport by wind: field studies at Owens Lake, California. *Earth Surface Processes and Landforms: The Journal of the British Geomorphological Group*, 23(1): 69–82.
- Laurent B, Marticorena B, Bergametti G, et al. 2005. Simulation of the mineral dust emission frequencies from desert areas of China and Mongolia using an aerodynamic roughness length map derived from the POLDER/ADEOS 1 surface products. *Journal of Geophysical Research: Atmospheres*, 110(D18), doi: 10.1029/2004JD005013.
- Lee H, Park S H. 2020. Stepwise assessment of different saltation theories in comparison with field observation data. *Atmosphere*, 11(1): 10, doi: 10.3390/atmos11010010.
- Li G, Zhang J, Herrmann H J, et al. 2020. Study of aerodynamic grain entrainment in aeolian transport. *Geophysical Research Letters*, 47(11): e2019GL086574.
- Li Z, Wu S, Dale J, et al. 2008. Wind tunnel experiments of air flow patterns over nabkhas modeled after those from the Hotan River basin, Xinjiang, China (I): non-vegetated. *Frontiers of Earth Science in China*, 2(3): 333–339.
- Lopez M V, Sabre M, Gracia R, et al. 1998. Tillage effects on soil surface conditions and dust emission by wind erosion in semiarid Aragon (NE Spain). *Soil and Tillage Research*, 45(1–2): 91–105.
- Marshall J K. 1971. Drag measurements in roughness arrays of varying density and distribution. *Agricultural Meteorology*, 8: 269–292.
- Marticorena B, Bergametti G. 1995. Modeling the atmospheric dust cycle: 1. Design of a soil-derived dust emission scheme. *Journal of Geophysical Research: Atmospheres*, 100(D8): 16415–16430.
- Marticorena B, Bergametti G, Gillette D, et al. 1997a. Factors controlling threshold friction velocity in semiarid and arid areas of the United States. *Journal of Geophysical Research: Atmospheres*, 102(D19): 23277–23287.
- Marticorena B, Bergametti G, Aumont B, et al. 1997b. Modeling the atmospheric dust cycle: 2. Simulation of Saharan dust sources. *Journal of Geophysical Research: Atmospheres*, 102(D4): 4387–4404.
- Marticorena B, Chazette P, Bergametti G, et al. 2004. Mapping the aerodynamic roughness length of desert surfaces from the POLDER/ADEOS bi-directional reflectance product. *International Journal of Remote Sensing*, 25(3): 603–626.
- Marticorena B, Kardous M, Bergametti G, et al. 2006. Surface and aerodynamic roughness in arid and semiarid areas and their relation to radar backscatter coefficient. *Journal of Geophysical Research: Earth Surface*, 111(F3), doi: 10.1029/2006JF000462.
- Mazzoli A, Moriconi G. 2014. Particle size, size distribution and morphological evaluation of glass fiber reinforced plastic (GRP) industrial by-product. *Micron*, 67: 169–178.
- Mu H, Otani S, Shinoda M, et al. 2013. Long-term effects of livestock loss caused by dust storm on Mongolian inhabitants: a survey 1 year after the dust storm. *Yonago Acta Medica*, 56(1): 39–42.
- Natsagdorj L, Jugder D, Chung Y S. 2003. Analysis of dust storms observed in Mongolia during 1937–1999. *Atmospheric Environment*, 37(9–10): 1401–1411.
- Onishi K, Otani S, Yoshida A, et al. 2015. Adverse health effects of Asian dust particles and heavy metals in Japan. *Asia Pacific Journal of Public Health*, 27(2): NP1719–NP1726.
- Otsu N. 1979. A threshold selection method from gray-level histograms. *IEEE Transactions on Systems, Man, and Cybernetics*, 9(1): 62–66.
- Raupach M R. 1992. Drag and drag partition on rough surfaces. *Boundary-Layer Meteorology*, 60(4): 375–395.

- Raupach M R, Gillette D A, Leys J F. 1993. The effect of roughness elements on wind erosion threshold. *Journal of Geophysical Research: Atmospheres*, 98(D2): 3023–3029.
- Schlichting H. 1936. Experimental investigation of the problem of surface roughness. In: National Advisory Committee for Aeronautics Collection. National Advisory Committee for Aeronautics, 1–34.
- Shao Y, Raupach M R, Findlater P A. 1993. Effect of saltation bombardment on the entrainment of dust by wind. *Journal of Geophysical Research: Atmospheres*, 98(D7): 12719–12726.
- Shao Y, Lu H. 2000. A simple expression for wind erosion threshold friction velocity. *Journal of Geophysical Research: Atmospheres*, 105(D17): 22437–22443.
- Shao Y. 2004. Simplification of a dust emission scheme and comparison with data. *Journal of Geophysical Research: Atmospheres*, 109(D10), doi: 10.1029/2003JD004372.
- Shao Y. 2008. *Physics and Modelling of Wind Erosion*. Dordrecht: Springer, 18–20.
- Shao Y, Ishizuka M, Mikami M, et al. 2011. Parameterization of size-resolved dust emission and validation with measurements. *Journal of Geophysical Research: Atmospheres*, 116(D8), doi: 10.1029/2010JD014527.
- Shao Y, Nickling W, Bergametti G, et al. 2015. A tribute to Michael R. Raupach for contributions to aeolian fluid dynamics. *Aeolian Research*, 19: 37–54.
- Tan L, Zhang W, Qu J, et al. 2013. Aeolian sand transport over gobi with different gravel coverages under limited sand supply: A mobile wind tunnel investigation. *Aeolian Research*, 11: 67–74.
- Tan L, Zhang W, An Z, et al. 2019. The effect of roughness density of gobi beds on the entrainment of sediment by wind: A wind tunnel study. *Journal of Wind Engineering and Industrial Aerodynamics*, 190: 183–189.
- Udo K. 2009. Field measurement of seasonal wind-blown sand flux using high-frequency sampling instrumentation. *Journal of Coastal Research*, SI(56): 148–152.
- Wang X, Xia D, Wang T, et al. 2008. Dust sources in arid and semiarid China and southern Mongolia: Impacts of geomorphological setting and surface materials. *Geomorphology*, 97(3–4): 583–600.
- Webb N P, Chappell A, LeGrand S L, et al. 2020. A note on the use of drag partition in aeolian transport models. *Aeolian Research*, 42: 100560, doi: 10.1016/j.aeolia.2019.100560.
- Wu C, Lin Z, Liu X. 2020. Global dust cycle and uncertainty in CMIP5 models. *Atmospheric Chemistry and Physics Discussions*, 2020: 1–52.
- Wu J, Kurosaki Y, Shinoda M, et al. 2016. Regional characteristics of recent dust occurrence and its controlling factors in East Asia. *SOLA*, 12: 187–191.
- Wu J, Kurosaki Y, Du C. 2020. Evaluation of climatic and anthropogenic impacts on dust erodibility: A case study in Xilingol Grassland, China. *Sustainability*, 12(2): 629, doi: 10.3390/su12020629.
- Xi X, Sokolik I N. 2015. Seasonal dynamics of threshold friction velocity and dust emission in Central Asia. *Journal of Geophysical Research: Atmospheres*, 120(4): 1536–1564.
- Yan Y, Xu X, Xin X, et al. 2011. Effect of vegetation coverage on aeolian dust accumulation in a semiarid steppe of northern China. *Catena*, 87(3): 351–356.
- Yang Y L, Victor S, Lu Q. 2002. *Global Alarm: Dust and Sandstorms from the World's Drylands*. New York: United Nations Pubns, 346.
- Zhang J, Teng Z, Huang N, et al. 2016. Surface renewal as a significant mechanism for dust emission. *Atmospheric Chemistry and Physics*, 16(24): 15517–15528.
- Zhang K, Zhang W, Tan L, et al. 2015. Effects of gravel mulch on aeolian transport: a field wind tunnel simulation. *Journal of Arid Land*, 7(3): 296–303.
- Zhang W, Tan L, Zhang G, et al. 2014. Aeolian processes over gravel beds: Field wind tunnel simulation and its application atop the Mogao Grottoes, China. *Aeolian Research*, 15: 335–344.